Journal of Materials Chemistry A

PAPER

View Article Online
View Journal | View Issue

Cite this: J. Mater. Chem. A, 2019, 7, 26540

Covalent organic framework-regulated ionic transportation for high-performance lithium-ion batteries†

Yucheng Wen,‡[a] Xianshu Wang,‡[a] Yan Yang,‡[a] Mingzhu Liu,[a] Wenqiang Tu,[a] Mengqing Xu,[ab] Gengzhi Sun,[ab] Seigou Kawaguchi,[c] Guozhong Cao*[d] and Weishan Li*[ab]

Separators of current lithium ion batteries (LIBs) based on transition metal oxide cathodes need to be highly conductive for lithium ions but not for transition metal ions (TMIs). Herein, a novel polymer separator that can regulate the transportation of lithium ions and TMIs is reported, and it is fabricated by coating a custom-designed covalent organic framework (COF) from 1,3,5-tris(4-aminophenyl) benzene and 2,5-dimethoxybenzene-1,4-dialdehyde on a commercial polymer separator (PS). Electrochemical measurements combining physical characterization demonstrate that the lithium ion transference number (t_{Li^+}) of the as-fabricated separator (PS@COF) is two times that of the uncoated PS, while the dissolved TMIs from cathodes are effectively isolated from anodes, leading to significantly enhanced cycling stability and rate capability of $Li[Li_{0.2}Mn_{0.55}Ni_{0.15}Co_{0.1}]O_2$ and $LiNi_{0.8}Co_{0.1}Mn_{0.1}O_2$-based LIBs. Theoretical calculations suggest that the COF provides the localized negatively charged groups ($-OCH_3$) for transporting lithium ions and the polar groups (–C=N–) with lone pair electrons for chelating TMIs. Our strategy shares a perspective for performance improvement of LIBs and holds great promise for the application of covalent organic frameworks (COFs) in energy storage and conversion.

Received 30th August 2019
Accepted 4th November 2019

DOI: 10.1039/c9ta09570e

rsc.li/materials-a

1. Introduction

The ever-growing energy consumption demands the exploration of new energy generation and storage technologies. Lithium-ion batteries (LIBs) are widely deployed in portable electronics, electric vehicles and smart electric grids.[1–5] The energy storage performances of LIBs are determined collectively by the electrodes, electrolyte and separator used, of which transition metal oxide cathodes such as layered lithium-rich[6] and nickel-rich[7] oxides are necessary to achieve high-energy-density LIBs.[8] As a crucial part in LIBs, a separator not only is responsible for separating the electrodes, but also serves as the reservoir for the electrolyte and mediates the transportation of ions.[9]

The common polyolefin-based (polypropylene (PP) or polyethylene (PE)) separator for LIBs allows lithium ions (Li^+) to pass through, accompanied by the permeation of other cations and anions. The cations are mainly nickel, cobalt, and manganese ions (collectively known as transition metal ions, TMIs), which dissolve from transition metal oxide cathode materials into electrolytes due to the phase transition-induced TMI disproportionation and the attack of acidic electrolytes.[10–12] These TMIs travel towards the anode due to the effect of the electric field, and then reductively deposit on the electrode surface, followed by the catalytic decomposition of the electrolyte, which increases the internal resistance from the stacking byproducts and deteriorates the performance of batteries due to overconsumption of the electrolyte.[13,14] Serious negative effects, including concentration polarization, reduced energy efficiency and joule heating, will compromise the battery performance, particularly during fast charge/discharge processes.[15] It is highly desirable to have separators that can suppress the penetration of TMIs but optimize the transportation of lithium ions.

Various strategies have been developed to suppress the dissolution of TMIs from cathodes with emphasis on tuning the interface/structural chemistry of cathodes. Surface coating with compounds such as ZnO, MgO[16] and $AlPO_4$,[17] bulk doping with elements such as Al,[18] Co,[19] and Ni,[20] and protective film construction with electrolyte additives are the

[a]School of Chemistry and Environment, South China Normal University, Guangzhou 510006, China. E-mail: liwsh@scnu.edu.cn

[b]National and Local Joint Engineering Research Center of MPTES in High Energy and Safety LIBs, Engineering Research Center of MTEES (Ministry of Education), Key Lab. of ETESPG (GHEI), South China Normal University, Guangzhou 510006, China

[c]Department of Organic Materials Science, Yamagata University, Yonezawa 992-8510, Japan

[d]Department of Materials Science and Engineering, University of Washington, Seattle, Washington 98195, USA. E-mail: gzcao@u.washington.edu

† Electronic supplementary information (ESI) available. See DOI: 10.1039/c9ta09570e

‡ These authors equally contributed to this work.

commonest ones to suppress TMI dissolution, but these approaches cannot ensure an efficient suppression of TMI dissolution from cathodes.[21–23] This is because doping cannot avoid the contact of the cathode materials with electrolyte, while the chemical/physical bonding between bulk materials and the coating/film layer is uneven. Separator modifications were also proposed to alleviate the detrimental effect of TMIs. For instance, Li *et al.* coated a commercial polyethylene separator with poly[divinylbenzene-(vinylbenzyl-aza-15-crown-5)-vinylbenzylchloride] to improve the high-temperature performance of $LiMn_2O_4$/graphite batteries and found that the identified manganese on the graphite anode was decreased from 10 to 5 μg cm^{-2} after 60 cycles at 0.2C and 50 °C.[24] Poly(vinylbenzo-18-crown-6) was also considered, which led to a decrease in the Mn content on the anode from 1.62 to 1.05 μg Mn per mg anode after 100 cycles at 0.25C and 60 °C.[25] Apparently, these modifications can suppress the transportation of TMIs through the separator to some extent, but the suppression is not efficient. Most importantly, these modifications might also block the transportation of lithium ions, which is unfavorable for the rate capacity delivery of LIBs. Recently, Zhang *et al.* reported a zirconium-based metal organic framework (MOF)-modified separator that could favor lithium ion transportation.[15] The lithium ion transference number (t_{Li^+}) was increased from 0.37 to 0.59 due to the anion immobilization of the MOF, although the transportation of TMIs was not taken into consideration in this report.

Covalent organic frameworks (COFs) that have controllable composition, topology and porosity[26–29] are receiving more and more attention in the field of energy storage. Xu *et al.* prevented the shuttle effect of lithium-sulfide intermediates by covalently engineering polysulfide chains on the pore walls of a COF.[30] Gu *et al.* adjusted the balance of the redox reactivity and stability of radical intermediates to optimize the electrochemical performance of sodium ion batteries using 2D COFs.[31] Inspired by the special functional groups of COFs, we synthesized a COF with 1,3,5-tris(4-aminophenyl)benzene (TPB) and 2,5-dimethoxybenzene-1,4-dialdehyde (DMTP) and fabricated a novel separator (PS@COF) by coating this COF on a commercial polymer separator (PS), to regulate the transportation of lithium ions and TMIs. This efficient regulation is attributed to the unique molecular structure of the COF, in which the localized negative charges stemming from the electron-withdrawing effect of the methoxy groups (–OCH_3) set a path for lithium ion transportation, while the polar groups (–C═N–) with lone pair electrons provide sites for chelating TMIs containing unoccupied orbitals (Fig. S1†). With such a regulation, the t_{Li^+} of the PS is significantly increased by two-fold, while the dissolved TMIs from cathodes are effectively isolated from anodes, leading to much better cycling stability and rate capability of $Li[Li_{0.2}Mn_{0.55}Ni_{0.15}Co_{0.1}]O_2$ and $LiNi_{0.8}Co_{0.1}Mn_{0.1}O_2$-based LIBs. Our strategy shares a perspective for performance improvement of LIBs, and holds great promise for the application of COFs in energy storage and conversion devices, not limited to LIBs.

2. Results and discussion

2.1 Characteristics of PS@COF

The XRD pattern of the as-synthesized COF shown in Fig. 1a can be well indexed to the COF,[29] which suggests an inorganic crystal structure with high purity. The inset in Fig. 1a gives the molecular structure of the COF, and the circle was formed by the strong covalence of subunits. FTIR spectra in Fig. 1b reveal absorption peaks at 3433 and 3354 cm^{-1} belonging to ν_{-NH_2} of TPB,[32] respectively. After growth, it transforms into $\nu_{-C=N}$ (1596 cm^{-1}) in the COF structure through its covalent reaction with –CHO of DMTP, which is associated with the vibration peak at 1679 cm^{-1} and it vanishes after the COF formation (Fig. 1b). As well, XPS analyses deliver the multi-component information of the COF (Fig. 1c–e). The C 1s spectra show two dominant peaks (Fig. 1c), including C–C at 284.8 eV and C–O at 286 eV. The corresponding C–O peak was also observed in the O 1s spectrum at 532.3 eV (Fig. 1d), while another one appearing at 533.7 eV was derived from benzene (Ar)–O. Additionally, the peak at 400.4 eV in the N 1s spectrum is attributed to C–N (Fig. 1e). These results demonstrate that the stable benzene-based unit and the polar –C═N bond can be preserved in the molecular structure of the COF. The Brunauer–Emmett–Teller (BET) analysis reveals the ultrahigh porosity of the COF, with a surface area of 2800 $m^2 g^{-1}$ and a pore size of 3.03 nm (Fig. 1f). Such a feature is conducive to the good uptake and storage of liquids.[15] Further, the TEM image gives a detail of the layer-arrangement structure of the COF with smooth edges (Fig. 1g). The morphology of the separator with COF modification is rich in void-parted nano-spheres, which closely arrange to form a network (Fig. 1i), compared to the commercial separator with irregular holes (Fig. 1h).

Density functional theory (DFT) calculations were performed to investigate the guided interaction of the COF with Li^+ and TMIs with various valences including Mn^{2+}, Mn^{3+}, Mn^{4+}, Co^{2+}, Co^{3+}, Co^{4+}, Ni^{2+}, Ni^{3+} and Ni^{4+}. The binding energy (E_b) and optimized structure are shown in Fig. 2; it can be found that the negative binding energies between the COF and TMIs with various valences are far surpassing that of COF and Li^+, indicative of the tendentious capture, by the COF, of these TMIs dissolved in electrolyte instead of the common Li^+. Surprisingly, it is observed that the C atom in the benzene ring adjacent to the –C═N bond tends to bind with Li^+, while the TMIs are bonded with the N atom in –C═N. This is the core of rationally COF-modified separators which can block the dissolved TMIs traveling to anodes while facilitating Li^+ migration. As proof, the deposition amounts of TMIs, including Ni, Co and Mn elements, on the lithium anode of $Li[Li_{0.2}Mn_{0.55}Ni_{0.15}Co_{0.1}]O_2$/Li cells using the PS and PS@COF after charge/discharge cycling were analyzed by ICP (Fig. S2†). The apparent difference significantly reflects that TMIs are isolated from the anode by PS@COF. The better isolation of TMIs from the anode by PS@COF can be more significantly observed in an H-type $Li[Li_{0.2}Mn_{0.55}Ni_{0.15}Co_{0.1}]O_2$/Li cell after cyclic voltammetry (Fig. S3†). Not only the TMIs are detected on the lithium plate but also the content increases after cycling with the PS.

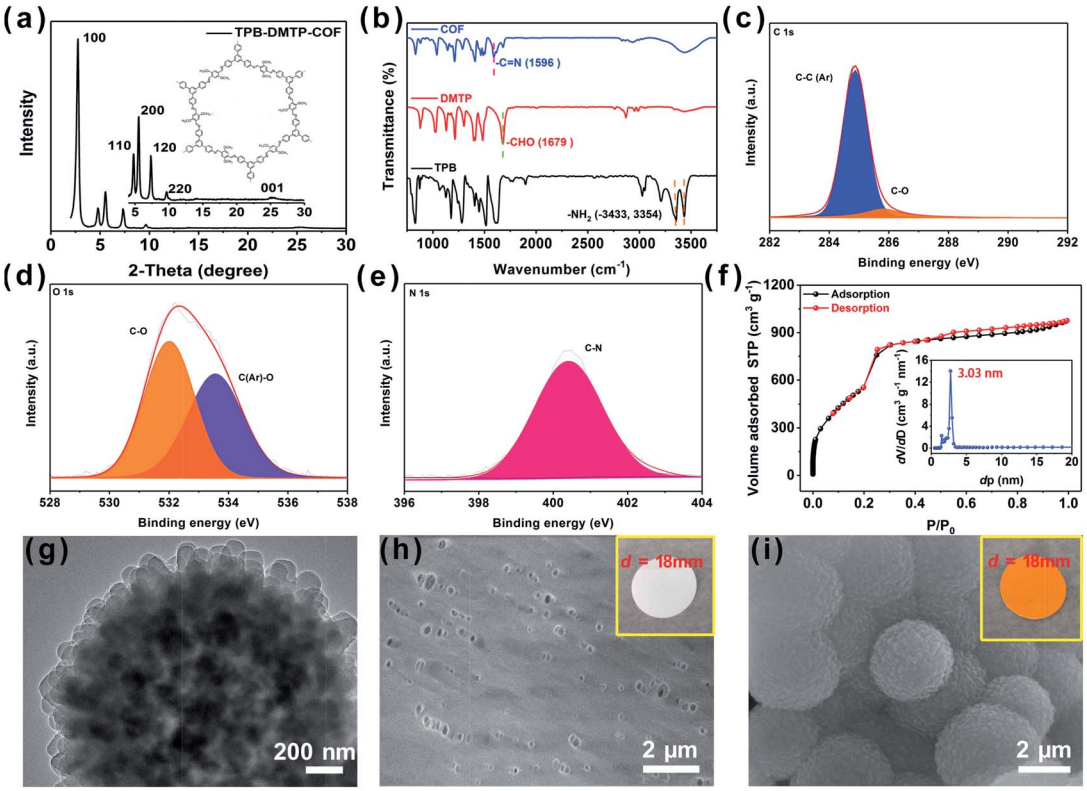

Fig. 1 Structural characterization. (a) XRD pattern and molecular structure of the COF. (b) FTIR spectra of TPB, DMTP, and the COF. (c–e) XPS spectra: (c) C 1s, (d) O 1s, and (e) N 1s in the COF. (f) Nitrogen adsorption/desorption isotherm of the COF. (g) TEM image of a COF nanoparticle. SEM images of commercial separators without (h) and with (i) COF modification.

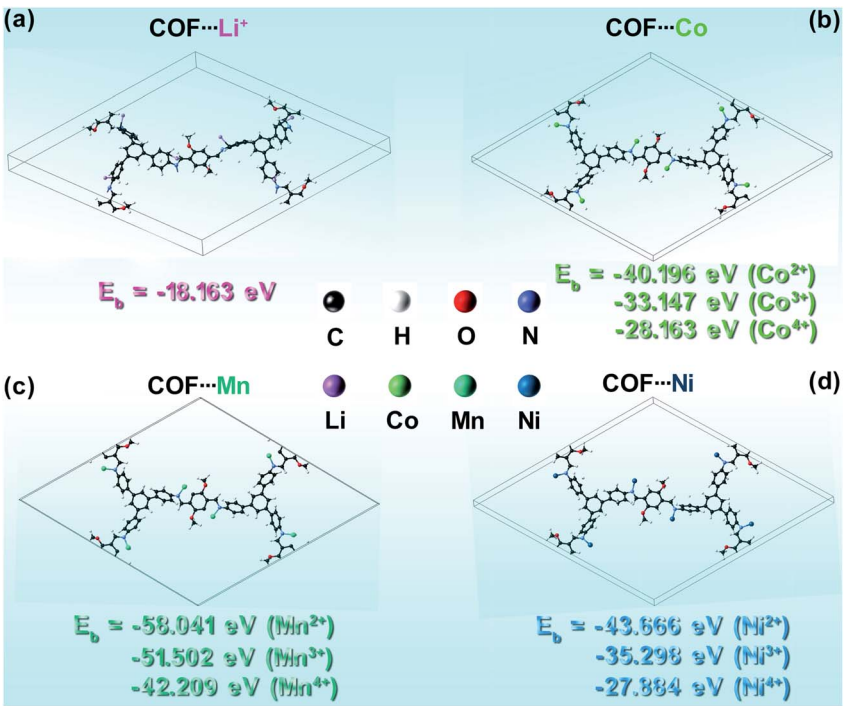

Fig. 2 Optimized structures and binding energy (E_b, eV) of the COF with X (X = (a) Li^+, (b) Co^{2+}, Co^{3+} and Co^{4+}, (c) Mn^{2+}, Mn^{3+} and Mn^{4+}, and (d) Ni^{2+}, $Ni^{3+}$and Ni^{4+}). The more negative the binding energy is, the stronger is the complexation of the COF with X.

However, no TMIs appeared on the lithium plate using PS@COF. It suggests that TMIs are not free to pass through the separator, indicating the efficient regulation of ion transportation by PS@COF.

The Li^+ transference number (t_{Li^+}) of the separators was determined with the classical Vincent–Bruce method. PS@COF presents a t_{Li^+} of 0.76, two times that of the PS (Fig. 3a, S4 and Table S1†), demonstrating that the COF favors Li^+ migration. The Coulomb force generated by the difference in electronegativity between O and C continuously pulls lithium ions between anode and cathode electrodes, which builds a special channel only for lithium ion migration. The construction mechanism of the lithium ion channel is shown in Fig. 3c. The electronegativity of O is stronger than that of C, causing the shared electron pair between O and benzene to shift toward O, which results in the C of the benzene being connected to $-OCH_3$ with a positive charge. Naturally, the C in the ortho position is negatively charged. A large number of sites in the COF are connected to form this highly selective channel for Li^+. The surface electrostatic potential map can prove that the ortho position of $-OCH_3$ carries a more negative potential, which provides a theoretical basis for the construction of the channel (Fig. 3d and e). The contribution of the COF to the improved Li^+ transference number of the separator can be verified by the effect of PVDF. When the PS was coated with PVDF rather than the COF, its t_{Li^+} decreased from 0.38 to 0.20 (Table S1†). Since the electrolyte solution contains only Li^+ cations and PF_6^- anions, an increased t_{Li^+} means the decrease of PF_6^- transference number. Consequently, the ionic conductivity of PS@COF is increased (Fig. S5 and Table S2†) and the concentration polarization will be reduced in LIBs. With such a feature of the COF, the cell with PS@COF exhibits a higher peak current of 9.33 mA cm^{-2} in contrast to the 4.73 mA cm^{-2} of the Li/PS/SS cell (Fig. 3b). Furthermore, no current responses in the following sweep up to 5.0 V for both the PS and PS@COF means that the incorporation of the COF does not affect the electrochemical stability of the electrolyte, and the COF is stable electrochemically on the SS electrode. The electrochemical stability of the COF can also be confirmed by charging/discharging the COF anode up to 0 V and the cathode up to 4.8 V in COF/Li cells (Fig. S6†) and identifying the structure of the COF after cycling a $Li[Li_{0.2}Mn_{0.55}Ni_{0.15}Co_{0.1}]O_2$/graphite full cell using PS@COF (Section 2.2). As shown in Fig. S6,† the COF does not exhibit lithium storage properties.

2.2 Effect of PS@COF on LIB performance

The effect of PS@COF on the performance of LIBs was evaluated using two typical TMI-based cathodes, $Li[Li_{0.2}Mn_{0.55}Ni_{0.15}Co_{0.1}]O_2$ (Li-rich) and $LiNi_{0.8}Co_{0.1}Mn_{0.1}O_2$ (NCM811). As Fig. 4a and S7† show, the $Li[Li_{0.2}Mn_{0.55}Ni_{0.15}Co_{0.1}]O_2$/Li cell with the PS presents a dramatic capacity decay with strongly fluctuating coulombic efficiency, although the initial cycling before 200 cycles maintains relative stability at 0.5C (1C = 200 mA h g^{-1}). This sudden capacity fading possibly derives from the drying up of the electrolyte due to serious catalytic decomposition on the anode in the presence of the travel of dissolved TMIs.[11] Eventually, it delivers a discharge capacity of only 59.5 mA h g^{-1} after 500 cycles, a retention of about 31.8%. In sharp contrast, a high capacity retention of 81.3% within the same cycles can still be contributed to by the cell with PS@COF, and the capacity drops slowly from the initial 202.9 to the final 164.2 mA h g^{-1}. In order to explore the decomposition of the electrolyte resulting from the catalysis

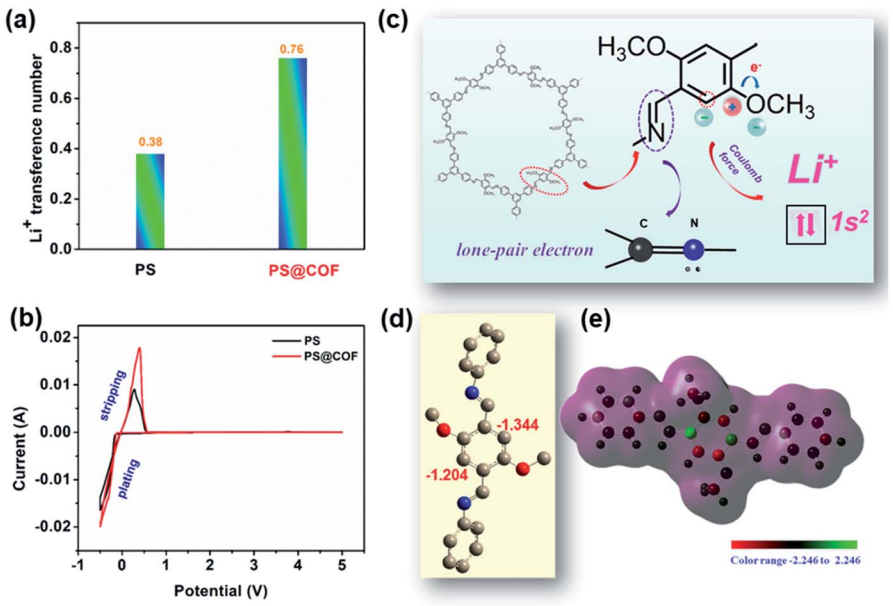

Fig. 3 (a) Comparison of Li^+ transference number between the PS and PS@COF at room temperature. (b) Cyclic voltammetric curves of SS/Li cells with the PS and PS@COF with a sweep rate of 1 mV s^{-1}. (c) Ionic transportation regulation mechanism of the COF-modified separator. (d) Optimized structure of the COF subunit and the distributed electronegativity on the adjacent carbon atom. (e) Surface electrostatic potential distribution of COF molecular fragments.

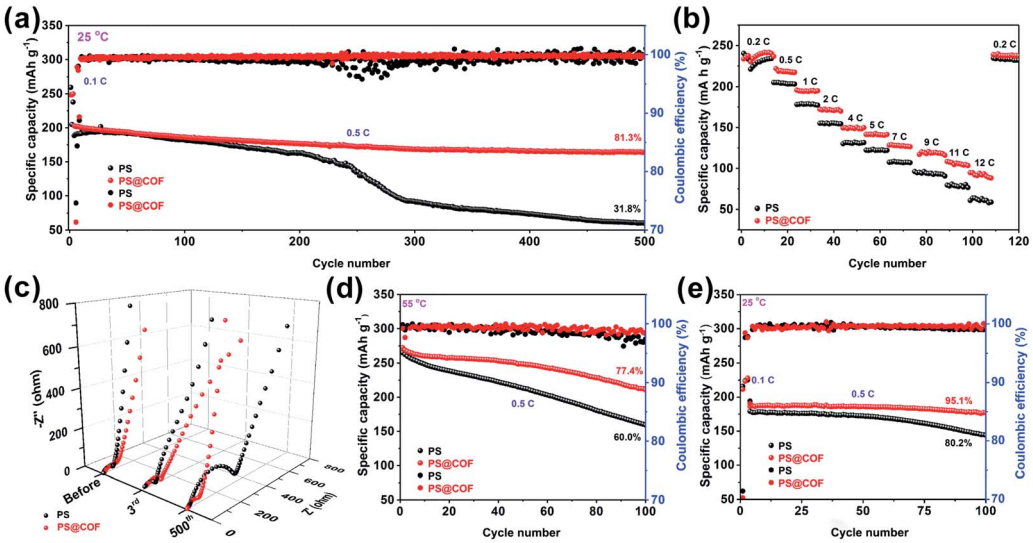

Fig. 4 Electrochemical performances of the PS and PS@COF. (a) Cycling stability at 0.5C, (b) rate capability at rates from 0.2 to 12C, and (c) electrochemical impedance spectra before cycling and after various cycles for $Li[Li_{0.2}Mn_{0.55}Ni_{0.15}Co_{0.1}]O_2$/Li cells with the PS or PS@COF as the separator at 25 °C. Cycling stability of (d) $Li[Li_{0.2}Mn_{0.55}Ni_{0.15}Co_{0.1}]O_2$/Li cells at a high temperature (55 °C) and (e) $Li[Li_{0.2}Mn_{0.55}Ni_{0.15}Co_{0.1}]O_2$/graphite batteries at 25 °C with the PS or PS@COF as the separator.

of TMIs, the morphology of the Li electrode after recycling is characterized by SEM (Fig. S8†). The surface of the Li electrode is covered with a thick and uneven decomposition product, but this product greatly reduces after the use of PS@COF. This indicates that PS@COF's selective permeability rejects the passage of TMIs, which can significantly alleviate the decomposition of electrolytes, thereby improving the performance of LIBs. It should be mentioned that the comparison of cycling stability shown in Fig. 4a is based on the same dosage of electrolyte solution (40 μL) for all the cells, suggesting that the better cycling stability of the cells using PS@COF than that using the PS is not caused by the different electrolyte uptake capabilities of the PS and PS@COF. A low dosage of the electrolyte solution (5 μL) leads to fast capacity decaying of the cell using the PS, while it does not change the cycling stability of the cell using PS@COF (Fig. S9†). Such an excellent cycling performance appearing in the $Li[Li_{0.2}Mn_{0.55}Ni_{0.15}Co_{0.1}]O_2$/Li cell using PS@COF rather than in the cell with the PS significantly highlights the effect of the COF, which suppresses the travel of dissolved TMIs from the cathode to the anode surface. As the discharge rates became larger, a more obvious difference can be observed between the discharge capacities of the $Li[Li_{0.2}Mn_{0.55}Ni_{0.15}Co_{0.1}]O_2$/Li cells using the PS@COF and PS (Fig. 4b), showing 240.3 mA h g^{-1} at 0.2C, 141.1 mA h g^{-1} at 5C and 93.2 mA h g^{-1} at 12C for the former compared to the 234 mA h g^{-1} at 0.2C, 122.2 mA h g^{-1} at 5C and 60.6 mA h g^{-1} at 12C for the latter. When the rate returned to 0.2C, they offer an approximate capacity delivery (237.3 *vs.* 232 mA h g^{-1}). This excellent rate performance is mainly determined by the superior t_{Li^+}.

Electrochemical impedance spectra taken during cycling showed constantly increasing interfacial impedance of the cells with the PS (Fig. 4c), demonstrating the accumulation of a thick SEI resulting from the catalytic decomposition of the electrolyte and finally the depletion of the electrolyte.[33] However, PS@COF can maintain a comparative interfacial stability for the cell thanks to the suppressed degradation of the electrolyte without the traveling TMIs on the anode and the good liquid preservation of the COF. At elevated temperatures, the lithium transition metal oxide cathode would suffer from more serious dissolution, migration and deposition of TMIs.[34] As shown in Fig. 4d, the fast capacity drop from 257.4 to 159.2 mA h g^{-1} can be observed in the $Li[Li_{0.2}Mn_{0.55}Ni_{0.15}Co_{0.1}]O_2$/Li cell with the PS within 100 cycles at 0.5C, with only 60% capacity retention. By contrast, the cells using PS@COF still achieve a capacity of 210 mA h g^{-1} at 0.5C after 100 cycles with a better coulombic efficiency (77.4% *vs.* 60.0%) and an increase of 17% in retention. This improved high-temperature cycling ability of the cathode containing transition metals further confirms the alleviation of the subversive effects of TMIs by the COF. Another supplementary cathode containing transition metals, lithium nickel cobalt manganese oxide (NCM811), can also harvest an improved long cycle life and cycling stability in the assembled cells with Li counterions, at ambient or high temperature (Fig. S10†).

As a down-to-earth application, the PS@COF should better be operated in graphite-based full cells due to the well-known adverse reaction of TMIs on graphite electrodes.[35] First, to exclude this doubt about graphite electrodes, graphite/Li cells with the PS and PS@COF were tested, with no interference from TMIs. The graphite/Li cells using the PS and PS@COF show no obvious difference in capacity delivery (Fig. S11†), which basically remains at 340 mA h g^{-1} at 0.2C (1C = 372 mA h g^{-1}) within 100 cycles. These results reveal that PS@COF does not affect the cycling stability of graphite electrodes. Fig. 4e shows the cycling performance of the $Li[Li_{0.2}Mn_{0.55}Ni_{0.15}Co_{0.1}]O_2$/graphite full cell at 0.5C and 25 °C. The capacity retention of the

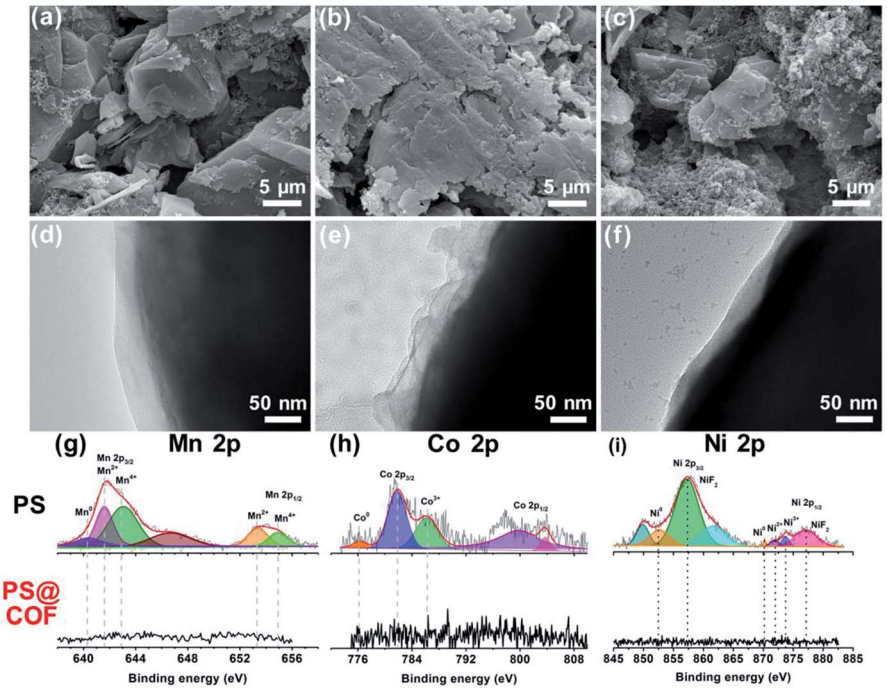

Fig. 5 Structural and surface chemistry analyses of graphite electrodes. (a–c) SEM and (d–f) TEM images of (a and d) fresh graphite and graphite electrodes cycled with the (b and e) PS and (c and f) PS@COF in the full cell. (g–i) XPS profiles of (g) Mn 2p, (h) Co 2p and (i) Ni 2p of the cycled graphite electrode with the PS and PS@COF.

full cell was significantly improved from 80% to 95% within 100 cycles in the presence of PS@COF (143.8 *vs.* 177.1 mA h g^{-1} in the last cycle). This demonstrates a successful case of using a COF as a separator coating for the travel-suppression of TMIs, which catalyze electrolyte decomposition and depletion, leading to thick SEI accumulation and increased internal resistance, and resulting in battery failure finally. The structural stability of the COF from the cycled cell using PS@COF, identified by XRD (Fig. S12†), demonstrates that the COF is stable electrochemically, particularly with such a cathode, $Li[Li_{0.2}Mn_{0.55}Ni_{0.15}Co_{0.1}]O_2$, and under a high voltage up to 4.8 V.

Fig. 5g–i show the difference of the relative transition metal species (Mn, Co, and Ni) on the cycled graphite electrodes with the PS and PS@COF separators. The peaks of Mn^0 (640.2 eV),[36] Co^0 (776.3 eV) and Ni^0 (852.5 eV)[37] are detected on the surface of graphite for the full cell with the PS, indicative of the undergone reduction and deposition of TMIs on anodes without the impeding COF. Moreover, the detected cations including Mn^{2+} (641.6 eV and 653.2 eV), Mn^{4+} (642.9 eV and 654.9 eV),[38,39] Co^{3+} (786.2 eV),[40] Ni^{2+} (872 eV)[41] and Ni^{3+} (873.7 eV)[42] not only disclose the traveling behavior of TMIs, but also lead to a conclusion that the common PS is not suitable for long-life batteries because of the hazards of TMIs. Another observation is the formation of NiF_2 (857.3 eV and 877.1 eV)[43] in Ni 2p spectra (Fig. 5i), which derives from the dissolved nickel ions catalyzing the decomposition of lithium salt ($LiPF_6$). For the graphite electrode in the PS@COF-based system, signals of Mn 2p, Co 2p and Ni 2p are not observed, which remarkably emphasizes the capture of TMIs by the COF. The other analyses of XPS spectra of C 1s, O 1s, F 1s and P 2p and the mapping of C, O, P, F, Mn, Co and Ni elements as well confirm the electrolyte decomposition and deposition of TMIs in the control system and their termination with the use of the COF in the separator (Fig. S13 and Table S3†). In other words, the content of TMIs on the surface of anodes using PS@COF has been greatly reduced, so that the half and full cells yield a much better electrochemical performance compared to those using the PS.

Based on the results and discussion above, the mechanism by which PS@COF improves the performance of lithium ion batteries can be schematically illustrated in Fig. 6. The common polyolefin-based separators for lithium ion batteries allow all ions to pass through as well as large solvation, leading to a low

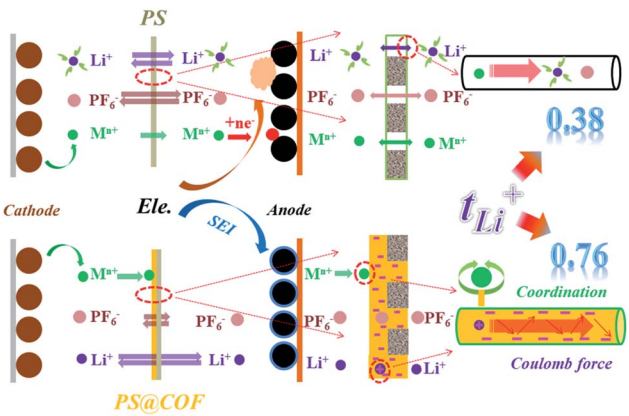

Fig. 6 Schematic illustration of the effect of PS@COF on the performance of a lithium ion battery.

t_{Li^+}. When the dissolved TMIs migrate to the anode, serious electrolyte decomposition is accelerated under their catalysis, eventually generating poor performance. The polar functional groups of PS@COF coordinate with TMIs to cut off the migration; moreover, the electron-withdrawing effect of the methoxy group (–OCH_3) empowers the ortho carbon atom with negative charge, accelerating the migration of lithium ions.

3. Conclusions

In summary, a polymer separator decorated with a proactively devised COF has been successfully developed for the improvement of lithium transition oxide-based batteries and the t_{Li^+} of separators. The as-engineered separator (PS@COF) exhibits promotion of t_{Li^+} as well as the ability to capture TMIs for suppressing their travel to the anode, which can be reduced into a metal element or can catalyze electrolyte degradation and enlarge the resistances, leading to capacity loss of batteries. The advantage derived from the structure of the COF endows the separator with ionically selective penetration. As a consequence, extraordinary electrochemical performances including long-term cycling ability and rate capability are harvested in lithium transition metal oxide cathode-based batteries, regardless of room temperature (25 °C) or elevated temperature (55 °C). It is believed that this selective COF design sheds light on a new perspective towards the modification of materials and structures for high-performance lithium batteries.

4. Experiment details

4.1 Materials preparation

The featured COF was synthesized by a typical crystal growth process. Typically, 0.224 g of 1,3,5-tris(4-aminophenyl)benzene (TPB) and 0.0186 g of 2,5-dimethoxybenzene-1,4-dialdehyde (DMTP) were dissolved in 1 mL of 1,4-dioxane and 1 mL of mesitylene, with the addition of 0.2 mL of 6 mol L^{-1} acetic acid. Then the mixture was kept in a quartz conical flask at 120 °C for three days under an argon atmosphere to obtain a yellow solid. Finally, the COF was obtained by washing the yellow solid 2–3 times with 1,4-dioxane, tetrahydrofuran and absolute ethanol, and drying in a vacuum oven at 85 °C for 12 h. The chemical regents used for synthesis were purchased from Zhengzhou Alpha Chemical Co., Ltd., China.

The COF-modified and PVDF-modified separators (PS@COF and PS@PVDF) were fabricated by a slurry-coating method. The as-synthesized COF and poly(vinylidenedifluoride) (PVDF) with a ratio of 8 : 2 by weight or the single component PVDF was dispersed in *N*-methyl pyrrolidone to form a slurry at room temperature. Then the different slurries were coated with a blade on a PS (Celgard 2400, BASF, $\varphi = 18$ mm, $d = 20$ μm) to form PS@COF and PS@PVDF ($\varphi = 18$ mm and $d = 60$ μm). Consequently, PS@COF contained 0.50–0.55 mg of COF.

Layered lithium-rich oxides ($Li[Li_{0.2}Mn_{0.55}Ni_{0.15}Co_{0.1}]O_2$) were synthesized by a co-precipitation method.[44,45] Typically, 2.1812 g of manganese sulfate ($MnSO_4 \cdot H_2O$), 1.0234 g of nickel nitrate hexahydrate ($Ni(NO_3)_2 \cdot 6H_2O$), and 0.6828 g of cobaltous nitrate hexahydrate ($Co(NO_3)_2 \cdot 6H_2O$) were dissolved in 50 mL of distilled water successively under continuous stirring, to obtain a mixed salt solution. Then, 1.654 g of lithium hydroxide ($LiOH \cdot H_2O$) and 3.69 g of ammonia were dissolved in 50 mL of distilled water as a precipitant solution. The above two solutions were dropped into a three-necked flask at a flow rate of 0.5 mL min^{-1} in a nitrogen atmosphere with stirring. After reacting at 50 °C for 12 h, the resulting precipitate was dried at 100 °C for 12 h. Then, the dried precursor and 1.2405 g of $LiOH \cdot H_2O$ were mixed under grinding. The resulting mixture was pre-heated in air at 500 °C for 5 h and then calcined in air at 900 °C for 12 h. The final product was obtained after uniform grinding. All the chemical regents for the synthesis were purchased from Shanghai Aladdin Biochemical Technology Co., Ltd., China. Another representative oxide, $LiNi_{0.8}Co_{0.1}Mn_{0.1}O_2$ (NCM811), was purchased from Ningbo Jinhe New Materials Co., Ltd., China.

Layered lithium-rich and NCM811 oxide cathodes, graphite anodes and COF electrodes were prepared. The slurry, consisting of $Li[Li_{0.2}Mn_{0.55}Ni_{0.15}Co_{0.1}]O_2$ or $LiNi_{0.8}Co_{0.1}Mn_{0.1}O_2$ or graphite (Ningbo Jinhe New Materials Co., Ltd., China), or COF, poly-(vinylidene difluoride) (PVDF) and acetylene carbon black (8 : 1 : 1 in weight), was coated on Al foil or Cu foil. The resulting foil was dried in a vacuum oven at 120 °C for 12 h, and then cut into a disk ($\varphi = 12$ mm). The loading mass of the active material for $Li[Li_{0.2}Mn_{0.55}Ni_{0.15}Co_{0.1}]O_2$/graphite full cells was calculated according to the *N*/*P* value of 1.2 (*N* and *P* are the specific capacities of the anode and cathode, respectively). The electrolyte solution for all the measurements in this work, 1.0 mol L^{-1} lithium hexafluorophosphate ($LiPF_6$) in a mixed solvent of diethyl carbonate (DEC), ethylene carbonate (EC), and ethyl methyl carbonate (EMC) (3 : 5 : 2 in weight), was provided by Guangzhou Tinci Materials Technology Co. Ltd. China. The ionic conductivity of this solution is 9.85 mS cm^{-1}. 40 μL of electrolyte solution was added to all the cells, except for special remark.

4.2 Measurements and characterization

The ionic conductivity (δ) of separators was measured in a symmetrical stainless steel (SS, $\varphi = 16$ mm) cell by electrochemical impedance spectroscopy (PGSTAT-30, Autolab Metrohm, Netherlands) at a voltage amplitude of 10 mV over a frequency range from 100 kHz to 1 Hz and calculated using the equation (eqn (1)):[46,47]

$$\delta = \frac{d}{R_b S} \quad (1)$$

where R_b is the bulk resistance, and d and S are the thickness and area of the separator, respectively.

The Li ion transference number (t_{Li^+}) was measured by potentiostatic polarization and electrochemical impedance spectroscopy on a Li/Li ($\varphi = 15.6$ mm) cell in electrolyte, and then calculated according to the Vincent–Bruce equation (eqn (2)):[48]

$$t_{Li^+} = \frac{I_{steady} \times \left(V - I_{initial} \times R_{int}^{initial}\right)}{I_{initial} \times \left(V - I_{steady} \times R_{int}^{steady}\right)} \quad (2)$$

where $I_{initial}$ and I_{steady} represent initial current and steady-state current recorded during potentiostatic polarization with a voltage bias (V), and $R_{int}^{initial}$ and R_{int}^{steady} represent the initial interfacial resistances before and after polarization, respectively. The polarization and the electrochemical impedance spectroscopy were performed on a Metrohm Autolab instrument. The voltage bias in the polarization test is 20 mV. The voltage amplitude is 5 mV and frequencies are from 500 kHz to 0.03 Hz for impedance measurements.

In order to test the ability of PS@COF to capture transition metal ions, an H-type $Li[Li_{0.2}Mn_{0.55}Ni_{0.15}Co_{0.1}]O_2$/Li cell was set up and cyclic voltammetry was performed with $Li[Li_{0.2}Mn_{0.55}Ni_{0.15}Co_{0.1}]O_2$ as the working electrode on a Solartron-1480 instrument (England) between 2 and 4.8 V (*vs.* Li/Li^+) under 0.1 mV s^{-1}. The effect of PS@COF on the performance of high energy density lithium-ion batteries was evaluated in half and full cells (2025 type). $Li[Li_{0.2}Mn_{0.55}Ni_{0.15}Co_{0.1}]O_2$/Li, NCM811/Li, graphite/Li and $Li[Li_{0.2}Mn_{0.55}Ni_{0.15}Co_{0.1}]O_2$/graphite cells were set up and charge/discharge cycling was performed on a LAND system (CT2001A, China). $Li[Li_{0.2}Mn_{0.55}Ni_{0.15}Co_{0.1}]O_2$/Li cells were charged and discharged between 4.8 and 2 V (*vs.* Li/Li^+) at 0.1C (1C = 200 mA h g^{-1}) for the first three cycles and at 0.5C for the remaining cycles. NCM811/Li cells were cycled between 4.35 and 3 V (*vs.* Li/Li^+) at 0.3C (1C = 180 mA h g^{-1}) for the first three cycles and at 1C for the remaining cycles. The graphite/Li cells were cycled between 0.005 and 2.5 V at 0.1C (1C = 372 mA h g^{-1}) for the initial three cycles and at 0.2C for the remaining cycles. $Li[Li_{0.2}Mn_{0.55}Ni_{0.15}Co_{0.1}]O_2$/graphite full cells were cycled between 2 and 4.8 V at 0.1C for the initial cycle and cycled at 0.5C in the subsequent cycles. Electrochemical impedance spectra of $Li[Li_{0.2}Mn_{0.55}Ni_{0.15}Co_{0.1}]O_2$/Li cells were obtained on a Metrohm Autolab instrument within a frequency range from 10^5 to 10^{-2} Hz and a voltage amplitude of 5 mV. For physical characterization, the electrodes were collected from the cycled cells in an Ar-filled glovebox and washed with DMC three times to remove residual electrolyte on the electrode surface.

The Brunauer–Emmett–Teller (BET) specific surface area and pore size were measured on a V-sorb 2800P (China) at 77 K. The content of transition metals deposited on the cycled lithium electrode was determined using an inductively coupled plasma atomic emission spectrometer (ICP-AES, Optima 8300, America). The electrode surface morphology of the cathode was observed by scanning electron microscopy (SEM, JSM 6510) and transmission electron microscopy (TEM, JEM-2100, JEOL, Japan). The organic functional groups in the COF were characterized by Fourier transform infrared spectroscopy (FTIR, Bruker Tensor 27, Germany) with a wavenumber from 500 to 4000 cm^{-1}. The surface composition of the electrodes and COF were determined by X-ray photoelectron spectroscopy (XPS, ESCALAB250, America).

4.3 Calculation details

Density functional theory (DFT) calculations were conducted using the Vienna *ab initio* Simulation package (VASP) and Gaussian 09 package. The projector augmented wave (PAW) method and the van der Waals density functional (vdW-DF) were adopted in DFT calculations. The energy cutoff was set to 520 eV. The self-consistent field (SCF) and geometry convergence tolerance were set to 1×10^{-5}. A $1 \times 1 \times 1$ k-point mesh was used in all systems for Brillouin zone integrations. The DFT+U approach was employed, where a $U_{eff} = U - J$ was added on the transition metal d states with U_{eff} (U_{eff} = 4.0, 3.3, and 6.4 eV for Mn, Co, and Ni).

The binding energy (E_b) was defined using the equation

$$E_b = E_{total} - E_{COF} - E_{ion} \quad (3)$$

where E_{total}, E_{ion} and E_{COF} are the total energies of the COF bound with Li^+, Mn^{4+}, Mn^{3+}, Mn^{2+}, Co^{4+}, Co^{3+}, Co^{2+}, Ni^{4+}, Ni^{3+} and Ni^{2+}, the single Li^+, Mn^{4+}, Mn^{3+}, Mn^{2+}, Co^{4+}, Co^{3+}, Co^{2+}, Ni^{4+}, Ni^{3+}, and Ni^{2+}, and the COF, respectively. The structure of the COF subunit optimized using Gaussian was used in the B3LYP method in combination with the 6–311++G (d) basis set.

Conflicts of interest

There are no conflicts to declare.

Acknowledgements

This work is financially supported by the National Key Research and Development Program of China (Grant No. 2018YFB0104000) and the Key Project of Science and Technology in Guangdong Province (Grant No. 2017A010106006).

Notes and references

1 M. Xu, L. Zhou, Y. Dong, Y. Chen, J. Demeaux, A. D. MacIntosh, A. Garsuch and B. L. Lucht, *Energy Environ. Sci.*, 2016, **9**, 1308–1319.
2 M. Li, J. Lu, Z. Chen and K. Amine, *Adv. Mater.*, 2018, **30**, 1800561.
3 T. Kim, W. Song, D.-Y. Son, L. K. Ono and Y. Qi, *J. Mater. Chem. A*, 2019, **7**, 2942–2964.
4 B. Liao, H. Li, M. Xu, L. Xing, Y. Liao, X. Ren, W. Fan, L. Yu, K. Xu and W. Li, *Adv. Energy Mater.*, 2018, **8**, 1800802.
5 B. Li, H. Yan, J. Ma, P. Yu, D. Xia, W. Huang, W. Chu and Z. Wu, *Adv. Funct. Mater.*, 2014, **24**, 5112–5118.
6 Y. Tian, M. Chen, S. Xue, Y. Cai, Q. Huang, X. Liu and W. Li, *J. Power Sources*, 2018, **401**, 343–353.
7 A. Manthiram, J. C. Knight, S.-T. Myung, S.-M. Oh and Y.-K. Sun, *Adv. Energy Mater.*, 2016, **6**, 1501010.
8 R. Schmuch, R. Wagner, G. Hörpel, T. Placke and M. Winter, *Nat. Energy*, 2018, **3**, 267–278.
9 M. F. Lagadec, R. Zahn, S. Müller and V. Wood, *Energy Environ. Sci.*, 2018, **11**, 3194.
10 X. Yang, J. Chen, Q. Zheng, W. Tu, L. Xing, Y. Liao, M. Xu, Q. Huang, G. Cao and W. Li, *J. Mater. Chem. A*, 2018, **6**, 16149–16163.
11 S. Wu, Y. Lin, L. Xing, G. Sun, H. Zhou, K. Xu, W. Fan, L. Yu and W. Li, *ACS Appl. Mater. Interfaces*, 2019, **11**, 17940–17951.

12 C. Wang, L. Xing, J. Vatamanu, Z. Chen, G. Lan, W. Li and K. Xu, *Nat. Commun.*, 2019, **10**, 3423.
13 C. Zhan, T. Wu, J. Lu and K. Amine, *Energy Environ. Sci.*, 2018, **11**, 243–257.
14 C. Zhan, J. Lu, A. Jeremy Kropf, T. Wu, A. N. Jansen, Y. K. Sun, X. Qiu and K. Amine, *Nat. Commun.*, 2013, **4**, 2437.
15 C. Zhang, L. Shen, J. Shen, F. Liu, G. Chen, R. Tao, S. Ma, Y. Peng and Y. Lu, *Adv. Mater.*, 2019, **31**, 1808338.
16 H. Sclar, O. Haik, T. Menachem, J. Grinblat, N. Leifer, A. Meitav, S. Luski and D. Aurbach, *J. Electrochem. Soc.*, 2012, **159**, A228–A237.
17 B. Xiao, B. Wang, J. Liu, K. Kaliyappan, Q. Sun, Y. Liu, G. Dadheech, M. P. Balogh, L. Yang, T.-K. Sham, R. Li, M. Cai and X. Sun, *Nano Energy*, 2017, **34**, 120–130.
18 X. Xiang, J. C. Knight, W. Li and A. Manthiram, *J. Electrochem. Soc.*, 2015, **162**, A1662–A1666.
19 D. Liu, X. Fan, Z. Li, T. Liu, M. Sun, C. Qian, M. Ling, Y. Liu and C. Liang, *Nano Energy*, 2019, **58**, 786–796.
20 F. Wu, J. Tian, Y. Su, J. Wang, C. Zhang, L. Bao, T. He, J. Li and S. Chen, *ACS Appl. Mater. Interfaces*, 2015, **7**, 7702–7708.
21 W. Tu, L. Xing, P. Xia, M. Xu, Y. Liao and W. Li, *Electrochim. Acta*, 2016, **204**, 192–198.
22 Q. Zheng, L. Xing, X. Yang, X. Li, C. Ye, K. Wang, Q. Huang and W. Li, *ACS Appl. Mater. Interfaces*, 2018, **10**, 16843–16851.
23 Y. Zhu, X. Luo, H. Zhi, Y. Liao and W. Li, *J. Mater. Chem. A*, 2018, **6**, 10994–11004.
24 Z. Li, A. D. Pauric, G. R. Goward, T. J. Fuller, J. M. Ziegelbauer, M. P. Balogh and I. C. Halalay, *J. Power Sources*, 2014, **272**, 1134–1141.
25 B. Ziv, N. Levy, V. Borgel, Z. Li, M. D. Levi, D. Aurbach, A. D. Pauric, G. R. Goward, T. J. Fuller, M. P. Balogh and I. C. Halalay, *J. Electrochem. Soc.*, 2014, **161**, A1213–A1217.
26 F. Beuerle and B. Gole, *Angew. Chem., Int. Ed.*, 2018, **57**, 4850–4878.
27 Y. Hu, N. Dunlap, S. Wan, S. Lu, S. Huang, I. Sellinger, M. Ortiz, Y. Jin, S. H. Lee and W. Zhang, *J. Am. Chem. Soc.*, 2019, **141**, 7518.
28 J. L. Segura, M. J. Mancheno and F. Zamora, *Chem. Soc. Rev.*, 2016, **45**, 5635–5671.
29 Q. Xu, S. Tao, Q. Jiang and D. Jiang, *J. Am. Chem. Soc.*, 2018, **140**, 7429–7432.
30 F. Xu, S. Yang, X. Chen, Q. Liu, H. Li, H. Wang, B. Wei and D. Jiang, *Chem. Sci.*, 2019, **10**, 6001–6006.
31 S. Gu, S. Wu, L. Cao, M. Li, N. Qin, J. Zhu, Z. Wang, Y. Li, Z. Li, J. Chen and Z. Lu, *J. Am. Chem. Soc.*, 2019, **141**, 9623–9628.
32 X. Wu, B. Wang, Z. Yang and L. Chen, *J. Mater. Chem. A*, 2019, **7**, 5650–5655.
33 D. Aurbach, M. Levi, K. Gamulski, B. Markovsky, G. Salitra, E. Levi, U. Heider, L. Heider and R. Oesten, *J. Power Sources*, 1999, **81**, 472–479.
34 W. Tu, C. Ye, X. Yang, L. Xing, Y. Liao, X. Liu and W. Li, *J. Power Sources*, 2017, **364**, 23–32.
35 R. Jung, F. Linsenmann, R. Thomas, J. Wandt, S. Solchenbach, F. Maglia, C. Stinner, M. Tromp and H. A. Gasteiger, *J. Electrochem. Soc.*, 2019, **166**, A378–A389.
36 D. Li, H. Li, D. L. Danilov, L. Gao, X. Chen, Z. Zhang, J. Zhou, R.-A. Eichel, Y. Yang and P. H. L. Notten, *J. Power Sources*, 2019, **416**, 163–174.
37 H. W. Nesbitt, D. Legrand and G. M. Bancroft, *Phys. Chem. Miner.*, 2000, **27**, 357–366.
38 J. Wang, Y. Yu, B. Li, T. Fu, D. Xie, J. Cai and J. Zhao, *Phys. Chem. Chem. Phys.*, 2015, **17**, 32033–32043.
39 Q. Li, G. Li, C. Fu, D. Luo, J. Fan, D. Xie and L. Li, *J. Mater. Chem. A*, 2015, **3**, 10592–10602.
40 D. Li, H. Li, D. Danilov, L. Gao, J. Zhou, R.-A. Eichel, Y. Yang and P. H. L. Notten, *J. Power Sources*, 2018, **396**, 444–452.
41 Z. Chen, J. Wang, D. Chao, T. Baikie, L. Bai, S. Chen, Y. Zhao, T. C. Sum, J. Lin and Z. Shen, *Sci. Rep.*, 2016, **6**, 25771.
42 D. McNulty, H. Geaney and C. O'Dwyer, *Sci. Rep.*, 2017, **7**, 42263.
43 A. N. Mansour, D. G. Kwabi, R. A. Quinlan, Y.-C. Lu and Y. Shao-Horn, *J. Electrochem. Soc.*, 2016, **163**, A2911–A2918.
44 C. Ye, W. Tu, L. Yin, Q. Zheng, C. Wang, Y. Zhong, Y. Zhang, Q. Huang, K. Xu and W. Li, *J. Mater. Chem. A*, 2018, **6**, 17642–17652.
45 M. Chen, X. Jin, Z. Chen, Y. Zhong, Y. Liao, Y. Qiu, G. Cao and W. Li, *J. Mater. Chem. A*, 2019, **7**, 13120–13129.
46 F. Chen, Y. Liao, M. Li, J. Huang, Q. Huang and W. Li, *J. Electrochem. Soc.*, 2018, **165**, A206–A214.
47 J. Liu, W. Li, X. Zuo, S. Liu and Z. Li, *J. Power Sources*, 2013, **226**, 101–106.
48 Z. Fu, H. Feng, C. Sun, X. Xiang, W. Wu, J. Luo, Q. Hu, A. Feng and W. Li, *J. Solid State Electrochem.*, 2013, **17**, 2167–2172.

